Aerothermodynamic Analysis of Aerocapture and Ballistic Entry Flows in Neptune's Atmosphere

João Alexandre Abreu Coelho
joao.alexandre.coelho@tecnico.ulisboa.pt

Instituto Superior Técnico, Lisboa, Portugal
Politecnico di Torino, Turin, Italy

December 2020

Abstract

Neptune is one of the Solar System's planets that are still unexplored. The engineering community must be prepared for the new challenges of a future mission to Neptune. For now, a lot of similarities are assumed between the atmospheres of Neptune and Jupiter. Specifically, the main components are believed to be molecular hydrogen and helium (in an approximate proportion of 80%/20%). However, Neptune's atmosphere is also believed to have methane (CH_4) in a small percentage (1.5%).

This work aims to evaluate the exact Neptune chemical composition (including CH_4) influence in the aerothermal environment of a capsule entering its atmosphere. Different capsule's shapes are considered ($60°$ and $45°$ sphere-cones), and two trajectory points for two different mission types are studied: a ballistic entry trajectory point (around 80km altitude at 18 km/s) an and aerocapture trajectory point (around 130km altitude at 29 km/s). For both capsules, different trajectory points and chemical compositions (with and without CH_4) are considered for the performed aerothermodynamic analysis, including both the convective and the radiative wall heat fluxes through the capsule's wall. The results show that, when the small percentage of methane is considered, the radiative wall heat fluxes increase significantly, particularly for the entry trajectory point.

Finally, a brief aerodynamic analysis is performed for the aerocapture trajectory point, evaluating the aerodynamic coefficients for capsules with trim tabs. The capsule with a cone angle $\theta = 45°$ seems to present better performance, whereas $\theta = 60°$ is prone to aerodynamic instabilities.

Keywords: Hypersonics, Aerocapture, Atmospheric Entry, Heat Fluxes, Radiation

1. Introduction

To learn more about our Solar system, one should know how most of its celestial bodies were formed. The human race has already (indirectly) visited a few asteroids, moons, and planets with this in mind. Many of them were even studied in depth. Nonetheless, there are still some doubts about many of our Solar system's celestial bodies, specifically the so-called Ice-Giants: Uranus and Neptune. Visiting them would most likely bring new information about their characteristics, providing us with a deeper insight into our Solar system as a whole.

It is known that Uranus and Neptune have an atmosphere composed of Helium, Hydrogen, with traces of Methane. Methane is responsible for the planets bluish color since it absorbs light in the wavelength corresponding to the red color in the visible spectrum. Neptune presents a darker blue tone compared to Uranus' greener tone (close to cyan), and the reason for this difference is not entirely known for now. This color difference is just one of many examples of the open questions about these planets. For these reasons, Neptune is already a strong candidate for a joint class-M NASA/ESA mission, aimed for 2030-2040 [1].

Multidisciplinary studies have already been made to assess the feasibility of a mission of this kind. Some of them consider aerocapture as the most efficient way of putting a spacecraft in a desired closed orbit around this blue planet [1].

1.1. Atmospheric Entry Overview

Due to a planet's strong gravitational well, an object entering through a planetary atmosphere like the one pictured in this work usually does so at very high entry velocities, with freestream Mach numbers well beyond Mach 5. The flow is hypersonic with the gas's internal energy being much smaller compared with its kinetic energy.

The capsules studied in this work will have a blunt body sphere-cone shape, which produces a near-normal shock at the nose region. This high-drag shape induces a strong bow-shock wave which will convert the coherent energy of the flow in thermal agitation energy. In turn, some of this agitation energy will be transferred to the species internal modes, leading to the onset of dissociation and ionization reactions. An advantage of the capsules' blunt-nose geometry is to allow for a certain amount of distance between the hot shock wave and the spacecraft surface, leading to decreased temperature gradients and, minimizing as much as possible the requirements for Thermal Protection Systems (TPS).

In the shock layer, endothermical chemical reactions, specifically dissociation reactions, start to occur as the temperature increases forming a partially ionized plasma around the capsule after the bow shock. All these chemical reactions emit/absorb radiation, a phenomena that may also be of great importance regarding the sizing of the capsule's TPS. We will study how much heat this radiation produces on the wall and if it is essential or not to try to mitigate this phenomenon.

Downstream of the post-shock equilibrium region, boundary layer and isothermal wall further cools the flow, allowing the recombination of several species. The environment is still severe though, and leads to the TPS ablation phenomena with a formation of an ablation layer of species constituted mostly by carbon. This phenomenon was not included in this work.

1.2. Neptune Mission

Visiting Neptune is a challenging task mainly because of its remote location in the Solar system. Minimum energy trajectories from Earth translate into a flight time of more than 30 years. There are ways to shorten this time, but this increases the entry velocity on Neptune's atmosphere. Reducing the trip time to 12-10 years could be possible and would reflect in entry velocities ranging from 29 to 32 km/s. [2]

As mentioned in [3], Neptune's aerocapture mission would aim to place a spacecraft into an elliptic orbit around Neptune, which would include regular flybys near Triton, one of Neptune's satellites. Since this satellite has a retrograde orbit direction, the entry trajectory would also include a retrograde entry path. This mission was also previously proposed by Jits *et al.* [2] and Hollis *et al.* [4]. Visiting Neptune (and Triton) is of great interest thanks to its proximity to the Kuiper Belt, which could increase our knowledge regarding the formation of the Solar system and the origin of life.

Usually, the orbit transfer is performed with a ΔV, generally achieved by reverse propulsion, to slow down the spacecraft. However, this option requires burning/ejecting a significant amount of propellant and is undesirable in terms of mission design.

One may instead take advantage of Neptune atmosphere, with the spacecraft skimming its upper layers and being decelerated by aerodynamic drag. This deceleration may be carried out slowly over a series of passes (aerobraking), or in a steep single maneuver (aerocapture). Both techniques require less fuel than the direct use of any all-propulsive maneuver. Some studies suggest that this type of approach may increase the mission's useful mass by at least 140%.

1.3. Capsule Design

Since the first atmospheric re-entry Space missions, the design adopted has been the sphere-cone shape blunt-body. The main reason is that this shape maximizes drag, allowing the spacecraft to decelerate as desired. Another important factor is related to wall heating.

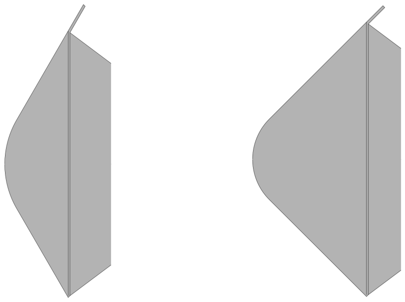

Figure 1: Capsule configurations ($\theta_c = 60°$ and $\theta_c = 45°$)

Two capsules configurations will be studied. See Figure 1. Both capsules will have a blunt-nosed conical (sphere-cone) outer model line, similar to the Galileo probe with two different cone-angles θ_c ($60°$ and $45°$). As mentioned in [5–7], typical Mars/Earth entry capsules with $60°$ / $70°$ half-cones are considered whereas $45°$ capsules are rather favored for gas giants. This work will focus on how these different configurations may affect the flow field, especially regarding wall heating, for this specific mission. Both capsules have a diameter of $D = 1.50\,m$. Nose radius, r_n, will be computed following the ratios $\left(\frac{r_n}{D}\right)$ proposed in the literature [1, 4]: $\left(\frac{r_n}{D}\right)_{60°} = 0.333$ and $\left(\frac{r_n}{D}\right)_{45°} = 0.205$. Table 1 summarizes the main parameters used for defining both capsules.

There was no interest in fully defining the capsule's aft body as the simulations only take into account the capsule's front and since the flow was expected to be supersonic when reaching the outlet, the expansion would not have any influence in the upstream flow. However, for $\theta_c = 60°$ Aerocapture Trajectory Point (TP) this was not the case, leading us to to further analysis regarding the sonic line stability in the flow. This will be discussed later.

All the simulations were performed with a cant angle of $0°$. The variation of the flap's sweep angle,

Table 1: Parametric values for the different capsules

θ_c	$60°$	$45°$
$D\,[m]$	1.50	1.50
$r_{nose}\,[m]$	0.500	0.308
A_{flap}/A_{main}	5%	5%

η, was studied, always keeping a ratio of frontal areas of the trim tab and the main body A_{flap}/A_{main} at 5%, see Figure 2.

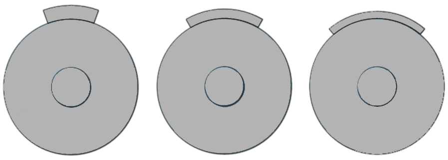

Figure 2: Different Sweep Angles η

2. Background

The literature regarding Neptune atmospheric entry remains sparse to this day. Most of the published work is related to Jupiter's entry since there is available data to be compared from the Galileo entry probe which successfully entered Jupiter in 1995. An example of this is legacy is the preliminary studies from ESA's CDF Study which consider a Galileo-like shape for the capsule and the same atmospheric composition than Jupiter. The influence of the trace components (CH_4) is not accounted for.

Some works do account for a more realistic atmospheric composition. In 2011, Park [3] analyzed the stagnation region of the flow from a blunt body performing an aerocapture in an atmosphere composed of a mixture of 81% H2, 17.5 % He, and 1.5 % CH_4 (molar fractions). The aerocapture trajectory point used was based on Hollis *et al.* [4] and Jits *et al.* [2], similar to those presented in the present work. Park considered the flow inviscid (without boundary layer), and focused on an analysis of chemical and radiative processes only for the stagnation line. A few years later, in 2014, Park [8] continued this work, but this time considering viscous phenomena with the presence of a boundary layer.

In this paper [3], the chemical dataset used considers C_3 and C_2H (neglected in the present work) and neglects the presence of C_2^+, H_2^+, He^+ (considered in the present work). Similar whe work done here, Park neglects the phenomenon of ablation. An assumption of constant pressure is further used, which overestimates the shock standoff distance by nearly 20% for a given nose radius. To correct this overestimation, the nose radius used in the computation is smaller than the actual nose radius, yielding to the correct shock standoff distance.

Hollis *et al.* [4] and Jits *et al.* [2] presented multidisciplinary studies regarding the convective and radiative heating for a Neptune Aerocapture Mission, which focused on topics such as aerothermodynamics, trajectory analysis, atmospheric modeling, aerodynamics, and structural design. In both these papers, although the capsule design is very different from the one used in the present work, there are a few results regarding the heating in the stagnation point which may be useful for comparison. The considered nose radius was 0.3m, which is similar to the $45°$ capsule from this work (0.308m). The trajectory points considered in these works were gathered for establishing a ground base helping to choose the aerocapture trajectory point used in this thesis.

Finally, ESA's Concurrent Design Facilities' (CDF) Study [1], yields a baseline analysis for a ballistic entry trajectory.

Even though the mentioned works present results at different altitudes, the present work will focus on two different trajectory points (TP) with the conditions described in Table 2.

Table 2: Freestream properties used in simulations

	Entry TP		Aerocapture TP
Cone angle θ_c	$60°$	$45°$	$60°$ /$45°$
V [km/s]	18.05	18.27	29
p [Pa]	698	892	145
ρ [kg/m^3] (x10^{-3})	2.996	4.229	0.378
T [K]	74.5	66.5	120.3
h (from 1 bar) [km]	82.3	77.3	130

3. Flowfield Modeling

This work exploits SPARK, a multi-physics CFD software designed for hypersonic flows with high temperature effects.

To obtain macroscopic properties of the flow around the capsule, the Navier-Stokes equations are solved, through the conservation equations that follows:

$$\frac{\partial(\rho c_s)}{\partial t} + \boldsymbol{\nabla}\cdot(\rho c_s \boldsymbol{V}) = \boldsymbol{\nabla}\cdot\boldsymbol{J_s} + \dot{w}_s \tag{1a}$$

$$\frac{\partial(\rho \boldsymbol{V})}{\partial t} + \boldsymbol{\nabla}\cdot(\rho \boldsymbol{V}\otimes\boldsymbol{V}) = \boldsymbol{\nabla}\cdot[\boldsymbol{\tau}] - \boldsymbol{\nabla} p \tag{1b}$$

$$\frac{\partial(\rho e)}{\partial t} + \boldsymbol{\nabla}\cdot(\rho \boldsymbol{V} e) = \boldsymbol{\nabla}\cdot(\boldsymbol{V}\cdot[\boldsymbol{\tau}]) - \boldsymbol{\nabla}\cdot(p\boldsymbol{V}) - \boldsymbol{\nabla}\cdot\boldsymbol{q} \quad , \tag{1c}$$

with the heat flux vector being a sum of diffusive heat and convective heat.

$$\boldsymbol{q} = \sum_s \boldsymbol{J}_s h_s - \sum_k \kappa_k \boldsymbol{\nabla} T_k$$

Radiative heat would also be included in this term, but in this work the radiative calculations are decoupled from the flowfield computations.

For each non-equilibrium thermal mode, an additional equation must be solved. For this work, a two-temperature model is employed with a vibrational temperature of H_2.

$$\frac{\partial(\rho e_{v,H_2})}{\partial t} + \boldsymbol{\nabla} \cdot (\rho \boldsymbol{V} h_{v,H_2}) = \boldsymbol{\nabla} \cdot \left(-\kappa_{v,H_2} \boldsymbol{\nabla} T_{v,H_2} + \sum_s \boldsymbol{J}_s h_{s,v,H_2} \right) + \dot{\Omega}_{v,H_2} \tag{1d}$$

3.1. Thermodynamics

Regarding the chemical composition of the freestream flow, two compositions were considered, and both are described in Table 3.

Table 3: Chemical compositions

	x_{H_2}	x_{He}	x_{CH_4}
A (with CH_4)	79.75 %	18.71 %	1.54 %
B (without CH_4)	81.00 %	19.00 %	0.00 %

The thermodynamic properties of the gas are computed from the classical high-temperature results of statistical thermodynamics.

3.2. Chemical Non-Equilibrium

To solve the flow considering the chemical non-equilibrium, a mass conservation equation must be solved separately for each species (1a).

The mass source term in this equation is modeled according to the relation expressing the net rate resulting from the forward and backward reactions.

$$\frac{\dot{w}_s}{\mathcal{M}} = \Delta\nu_{s,r} \left\{ k_{f,r} \prod_s [X_s]^{\nu'_{s,r}} - k_{b,r} \prod_s [X_s]^{\nu''_{s,r}} \right\} \tag{2}$$

The forward reaction rate can be obtained from the Arrhenius equation and $k_{b,r}$ is computed from the equilibrium constant.

Several models may be established for H_2/He/CH_4 mixtures. The one chosen for this work was selected from two reference models: Report from Lino da Silva [9] (for Titan's atmospheric entries, which focused on validating rates from Gökçen's work [10]) and the work from Leibowitz and Kuo [11] (experimentally determined rates for an H_2/He mixture). The resulting kinetic dataset is presented in Table 4. Obviously, for the chemical composition B (without CH_4), the chemical reactions with carbonaceous species are ignored.

Table 4: Chemical Model used in the present work

		Reaction		Ref.
R1	$H + H$	$\longleftrightarrow$	$H^+ + e^- + H$	[11]
R2	$H + He$	$\longleftrightarrow$	$H^+ + e^- + He$	[11]
R3	$H_2 + M$	$\longleftrightarrow$	$H + H + M$	[9]
R4	$CH_4 + M$	$\longleftrightarrow$	$CH_3 + H + M$	[9]
R5	$CH_3 + M$	$\longleftrightarrow$	$CH_2 + H + M$	[9]
R6	$CH_3 + M$	$\longleftrightarrow$	$CH + H_2 + M$	[9]
R7	$CH_2 + M$	$\longleftrightarrow$	$CH + H + M$	[9]
R8	$CH_2 + M$	$\longleftrightarrow$	$C + H_2 + M$	[9]
R9	$CH + M$	$\longleftrightarrow$	$C + H + M$	[9]
R10	$C_2 + M$	$\longleftrightarrow$	$C + C + M$	[9]
R11	$CH_3 + H$	$\longleftrightarrow$	$CH_2 + H_2$	[9]
R12	$CH_2 + H$	$\longleftrightarrow$	$CH + H_2$	[9]
R13	$CH + C$	$\longleftrightarrow$	$C_2 + H$	[9]
R14	$C + H_2$	$\longleftrightarrow$	$CH + H$	[9]
R15	$H + CH_4$	$\longleftrightarrow$	$CH_3 + H_2$	[9]
R16	$H + H$	$\longleftrightarrow$	$H_2^+ + + e^-$	[9]
R17	$C + H$	$\longleftrightarrow$	$CH^+ + e^-$	[9]
R18	$C + C$	$\longleftrightarrow$	$C_2^+ + e^-$	[9]
R19	$H + e^-$	$\longleftrightarrow$	$H^+ + e^- + e^-$	[11]
R20	$He + e^-$	$\longleftrightarrow$	$He^+ + e^- + e^-$	[11]
R21	$C + e^-$	$\longleftrightarrow$	$C^+ + e^- + e^-$	[9]
R22	$H_2 + e^-$	$\longleftrightarrow$	$H_2^+ + e^- + e^-$	[9]
R23	$CH + e^-$	$\longleftrightarrow$	$CH^+ + e^- + e^-$	[9]
R24	$CH^+ + e^-$	$\longleftrightarrow$	$C^+ + H + e^-$	[9]
R25	$CH^+ + e^-$	$\longleftrightarrow$	$C + H^+ + e^-$	[9]
R26	$C_2 + e^-$	$\longleftrightarrow$	$C_2^+ + e^- + e^-$	[9]
R27	$H_2^+ + e^-$	$\longleftrightarrow$	$H^+ + H^+ + e^- + e^-$	[9]
R28	$CH^+ + e^-$	$\longleftrightarrow$	$C^+ + H^+ + e^- + e^-$	[9]
R29	$H_2^+ + e^-$	$\longleftrightarrow$	$H + H$	[11]

3.3. Thermal Non-Equilibrium

A two-temperature model was employed for thermal non-equilibrium allowing the vibrational energy levels of H_2 to be populated according to a Boltzmann distribution at a temperature T_{v,H_2}. The remaining thermal modes are assumed to be at a different temperature, T_{tr}. In the radiative analysis, both T_{e^-} and T_{v,H_2} are assumed in equilibrium, as vibrational and electronic energy modes exchange energies very efficiently.

Vibrational relaxation times are obtained from Millikan-White's correlation, with coefficients provided by Palmer *et al.* [12].

3.4. Transport

This work used the updated and improved Gupta/Yos formulation from SPARK implemented by Santos Fernandes [13]. The Gupta/Yos model is known to be more accurate than the Wilke/Blottner/Eucken model which considers the Collisional Cross Sections (CCS) as a constant for all species. This latter model presents significant inaccuracy for higher temperatures, typical of the flowfields presented in this work, and thus was discarded. For the solutions without CH_4 (chemical composition B), a *2nd order model* was used, consisting on considering the non-diagonal terms of the Chapman-Enskog formulation. However, when the number of chemical species was raised from 7 to 16, the CFD code experienced a significant decrease in efficiency, forcing us to turn off this feature.

4. Radiation Modeling

4.1. Radiative Transfer Models

Radiative energy is transferred at the speed of light through all the lines of sight of a gas emitting this radiation.

Based on the Radiative Transfer equation, the following solution can be obtained

$$I_\nu^{\theta,\phi}(L) = I_{\nu,0}^{\theta,\phi} e^{-\tau_\nu(L)} + \int_0^{\tau_\nu(L)} \frac{j_\nu}{\kappa_\nu} e^{-(\tau_\nu(L)-\tau_\nu)} d\tau_\nu . \quad (3)$$

Equation (3) expresses the radiative spectral intensity as function of spectral coefficients (j_{nu} and κ_{nu}) and optical thickness ($\tau_\nu = \int_0^s \kappa_\nu ds'$) at a position L in the line of sight defined by the direction (θ, ϕ).

Integrating $I_\nu^{\theta,\phi}$ over the different hemispherical directions and over the spectral domain, we obtain $I_\nu^{\theta,\phi}$ for each point. For each wall point, integrating over every directional intensity we obtain the radiative heating

$$q_{rad} = \int_0^\infty \int_0^{2\pi} \int_0^\pi I_\nu^{\theta,\phi} \cos\theta \sin\theta \, d\theta \, d\phi \, d\nu \quad . \quad (4)$$

To solve equation (4), different approaches may be used. Particularly there are two models usually implemented in the scientific community: Tangent Slab and Ray Tracing.

The Tangent Slab approach lies under the approximation of the flow properties being considered to vary only in the directional normal to the body. This is the same as considering the flow field normal to the point being computed to be extended to infinity. This is a simplified approach, which overpredicts the radiative heats, but still yields a good approximation. The computational cost is less than the one with the Ray Tracing since there is only one ray that needs to be integrated (the normal one to the surface).

Ray Tracing models yields more accurate results since they are closer to a physical approach to the problem. After discretizing the rays, the equations are solved along a given ray between the upstream and the wall boundaries followed by a spatial integration of each ray and frequency.

There are several ways to discretize the spatial domain over the different rays chosen. The simplest way is to discretize considering a Latitude-Longitude lattice, with constants $\Delta\theta$ and $\Delta\phi$. A better approach is to consider a Fibonacci Lattice [14], that guarantees a uniform distribution of points over a specific spherical surface. Both lattices are represented in Figure 3.

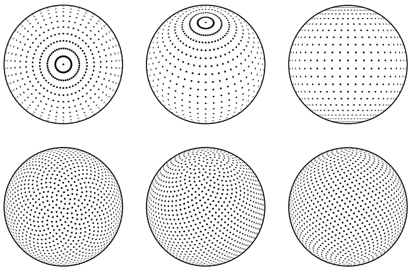

Figure 3: Latitude-Longitude (top) vs Fibonacci lattice (bottom) (Adapted from [14])

The total number of rays per hemisphere is also a quantity that can be changed. Several convergence exercises made for this work concluded that increasing from 50 to 100 rays provided a 2% difference in the overall results for the radiative heat flux along the wall, but had significant impact on computational times, with times increasing by almost a factor of 2.5. Another test was done to analyze this convergence but only for the stagnation wall point. Compared with choosing 1500 rays, the case with 50 rays resulted only in an error of 2.36%, and again, this increase of rays resulted in significant increase of computational times. For this reason, the remaining analysis was performed using 50 rays per hemisphere.

Following the rays discretization we compute the emission and absorption coefficients on each line of sight from the temperature and species' number densities distributions. Each ray will intercept cells in points different than the cells center. A choice must be made in how the coefficients will be integrated over a specific cell. One option is to consider constant parameters throughout the cell, with resulting discontinuities in the cell boundaries. This can reduce the accuracy of the resulting radiative intensity of a ray while integrating through coarse cells. Another option is to linearly interpolate the radiative coefficients, considering the adjacent cells.

The linear interpolation method comes with a significant increase of computational effort, with computational times becoming 10x larger for reaching one solution. For this reason, we chose not to use this interpolation, after performing a test with two cases, and confirming that the error associated with this was smaller than 2.5% in one case and 0.5% in the other. The significant increment in the computational times, did not reflect in significant changes in the results.

4.2. Radiative Database

The deployed spectral database included in the following radiative systems:

- Atomic Lines : H, He, He^+, C, C^+
- Atomic Photoionization: H, He, He^+, C, C^+
- Atomic Photodettachment: H^-, He^-, C^-
- Molecular Photoionization: H_2
- Molecular Photodissociation: H_2, H_2^+
- Bremsstrahlung: H, He, He^+, C, C^+, H_2^-
- Molecular Band Systems:

H_2

- Lymann
- Werner
- Fulcher
- B' - X
- D - X
- B"B - X
- D' - X

C_2

- Freymark
- Phillips
- Mulliken
- Herzberg - F
- Herzberg - g
- Herzberg - f
- Swan
- Deslandres - d'Azambuja
- Fox Herzberg
- Ballik Ramsay

5. Results & Discussion

In both test cases, the mesh defined for both capsule designs went through a preliminary mesh convergence study. All defined meshes had refinements brought both on the shock as well as on the boundary layer, where first cell height (defined as $Re_{wall} = \frac{\rho_w a_w \Delta n}{\mu_w} > 20$) was never larger than 2 μm, a compromise between accuracy and simulation run-times. Also, since the transport model used was Gupta-Yos (and not Wilke's), the boundary layer is believed to be accurately modeled, as shown in [13].

5.1. Test Case 1

An aerothermodynamic analysis for two different trajectory points (Entry TP and Aerocapture TP) and for the two capsule geometries is carried out. For each of these trajectory points, both chemical compositions (presented in Table 3) will be analyzed, studying the influence of the marginal presence of CH_4 in the results. Table 5 summarizes the corresponding test matrix. The analysis will focus on the convective and radiative heating.

Table 5: Test matrix for Test Case 1

Cone angle θ_c	Trajectory Point	Chemical Composition
60°	Entry TP	A (with CH_4) B (without CH_4)
45°	Entry TP	A (with CH_4) B (without CH_4)
60°	Aerocapture TP	A (with CH_4) B (without CH_4)
45°	Aerocapture TP	A (with CH_4) B (without CH_4)

A detailed analysis of the chemistry and radiative systems is performed in the stagnation line and compared between the different cases. Figure 4 presents the differences in the stagnation line temperature for all cases.

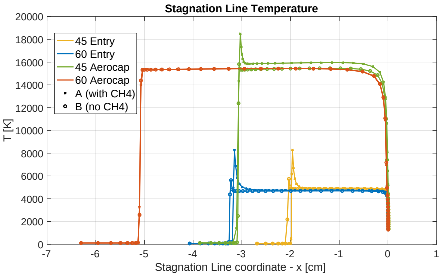

Figure 4: Stagnation Line Temperatures - all cases

Analyzing the top radiative systems for the Entry TP, the most prominent systems on the stagnation line for the chemical composition A are issued from C_2 (with the top 5 being Deslandres d'Azambuja, Fox Herzberg, Swan, Ballik Ramsay and Phillips). Besides the C_2 species, the next more important radiative system come from H, with H (Atomic) as the most important for this species. For the chemical composition B, the most important radiative systems are H (Atomic), H (Bremststrahlung) and H_2 (PhotoDissociation).

Taking this into account, one may explain the different behavior of the wall radiative heat fluxes along the wall for each case:

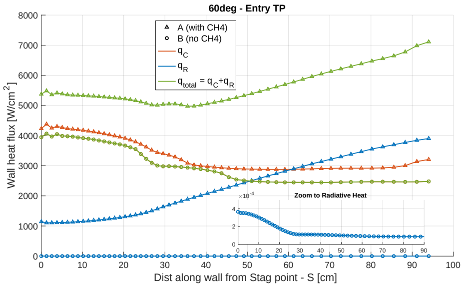

(a) θ_c=60°

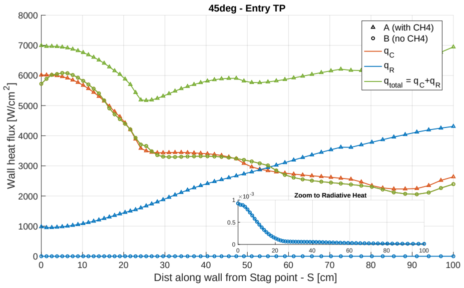

(b) θ_c=45°

Figure 5: Wall Heat Fluxes - Entry TP

- For the Entry TP, considering a chemical composition A (with CH_4), the most dominant radiative transitions belong to the C_2 species (the top 5 systems). This species is present throughout the whole domain, with a particular growth in molar fractions as we get farther from the stagnation region, which yields additional radiative emissivity in this spatial region. Figure 6 confirms this line of thought, with the significant contribution to the cumulative heat flux (from the spectral integration) coming from wavelengths correspondent to C_2 radiative systems. Without CH_4 (composition B), the most dominant radiative transitions come from H (Atomic). Contrarily to C_2 for composition A, the atomic hydrogen concentrations are higher on the stagnation region. Figure 7 confirms this, with the significant contribution to the cumulative heat flux (during the spectral integration) coming from wavelengths correspondent to H atomic lines, and being more significant in the stagnation region. This is also enhanced by the large temperatures in this region.

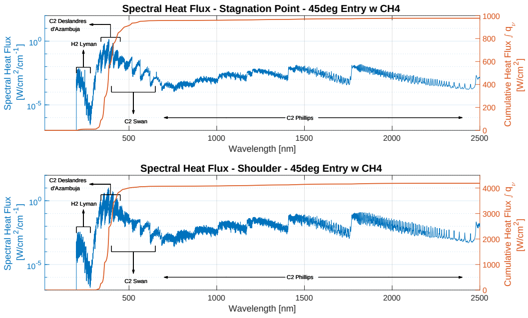

Figure 6: Spectral Heat Fluxes - Entry TP with CH_4

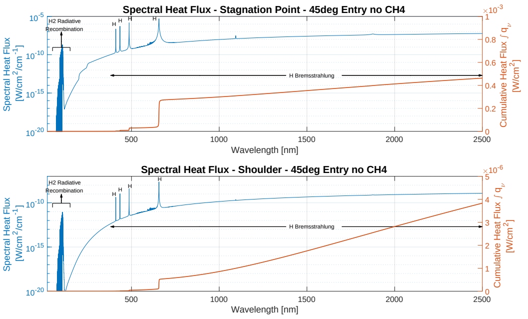

Figure 7: Spectral Heat Fluxes - Entry TP without CH_4

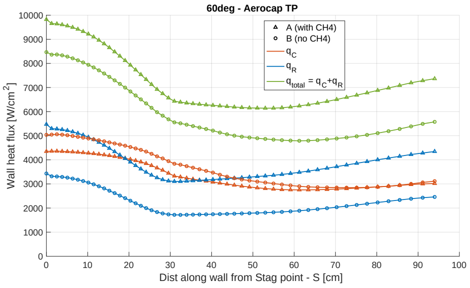

(a) θ_c=60°

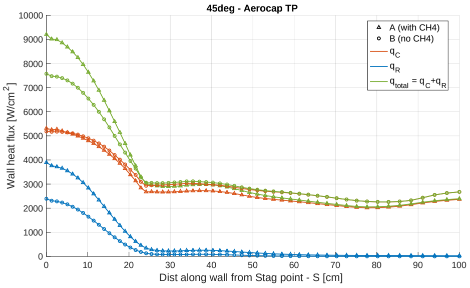

(b) θ_c=45°

Figure 8: Wall Heat Fluxes - Aerocapture TP

- For the Aerocapture TP, the dominant radiative systems are from H and C atomic lines. For this trajectory point, the higher temperatures preclude the significant presence of molecules such as C_2 which is why this species is no longer dominant in the radiation. Also, as we get farther from the stagnation region, even though there is no significant change in the species molar fractions (as there was for the C_2 in the previous TP), there is a significant change in the temperature field. With the higher velocity from this trajectory point, the difference between the oblique shock and a normal shock is more important, which yields significant changes in the post-shock temperatures of the stagnation region (where the shock is closest to a normal shock) and the conical part of the capsule (where the shock is an oblique shock). The higher the temperature, higher the radiative power of H and C atomic radiative systems. For this reason, in the stagnation region, the radiative power will be higher, yielding higher radiative heat fluxes in this region. Figure 9 confirms this rationale, with the most significant contribution to the cumulative heat flux (from the spectral integration) coming from wavelengths correspondent to H and C atomic lines radiative systems. This contribution is higher in the stagnation region, where these species are at higher temperatures, and emit more radiation. For this trajectory point, the dominant radiative systems are from H and H_2, and there are no significant changes when considering the two different chemical compositions (A and B) as these species are present in both of them. Figure 10 shows a significant difference in the spectral heat flux component (blue) compared to Figure 9. Most of the lines disappear since most of them corresponded to C atomic lines.

Literature comparison

For both trajectory points, a few studies were considered for comparison purposes. A straightforward comparison is not possible since the conditions used in this work were not exactly the same as the ones in comparison. These were made just for confirming a trend (or lack of) of the results there obtained.

ESA's CDF Study [1] is a multidisciplinary study focused on a mission to Neptune. Some studies were made regarding an atmospheric entry us-

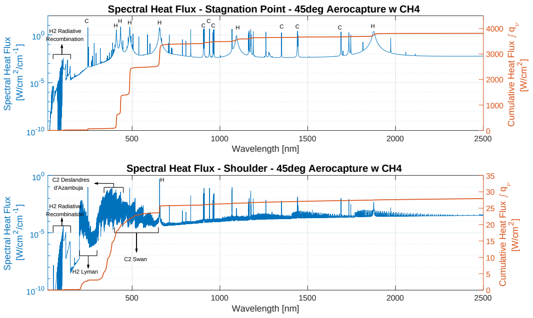

Figure 9: Spectral Heat Fluxes - Aerocapture TP with CH_4

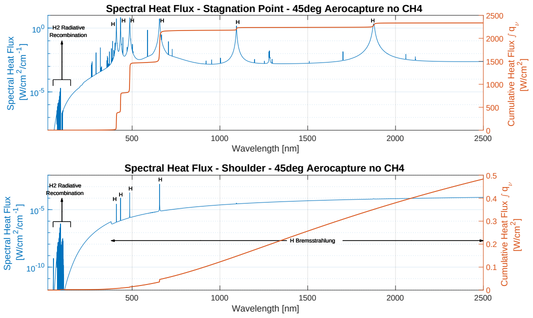

Figure 10: Spectral Heat Fluxes - Aerocapture TP without CH_4

ing a Galileo-Like capsule, with a nose radius of 0.370m, relatively similar to the nose radius from this work's capsule with $\theta_c = 45°$, r_n=0.308m. The presented results were obtained using correlations based on Simmonds and Moss's simulations [15] without using any CFD techniques. Discrepancies in the freestream properties also make a straightforward comparison to be inadequate.

Nevertheless, there is not a significant scattering of the results shown in Table 6, showing them to be reasonable for the performed simulations.

Table 6: Comparison for Entry TP $\theta_c = 45°$

		q_C	q_R	V$_\infty$	P$_\infty$	r_n
		[W/cm^2]		[km/s]	[Pa]	[m]
ESA's CDF [1]		3801	965	18.77	276	0.370
45 Entry	no CH_4	5723	~ 0	18.27	892	0.308
	w CH_4	6014	978			

For the Aerocapture TP, Hollis et. al [4], and Park [3, 8] performed an aerothermodynamic analysis, using Viscous Shock Layer (VSL) simulations, which is 1D stagnation streamline CFD model. The nose radius used was not the "true" nose radius of 0.5m but instead an equivalent nose radius that would result in the same shock stand-off distance as the simulations from Hollis *et al.* [4], where the nose radius of the spacecraft was 0.5m. This is the same as the one used in this work for $\theta_c = 60°$. Hollis *et al.* performed 3D simulations for a capsule with a very distinct shape compared to the one used here. This said, these are not meant to be straightforward comparisons, but instead meant to confirm the order of magnitude of our results.

Even though the results presented in Table 7 are not similar between these cases, the overall order of magnitude is the same, which makes this work's results acceptable.

Table 7: Comparison for Aerocapture TP $\theta_c = 60°$

	q_C	q_R	V$_\infty$	T$_\infty$	r_n
	[W/cm^2]		[km/s]	[K]	[m]
Hollis *et al.* [4]	3833	1300	27.7	103	0.5
Park (viscous) [8]	N/A	3215	27.7	103	0.5
Park (inviscid) [3]	N/A	2800	27.7	103	0.5
60 Aeroc. (no CH_4)	5036	3432	29	130	0.5
60 Aeroc. (w CH_4)	4349	5295			

Sonic line instabilities

A unexpected result for the case of Aerocapture TP with $\theta_c = 60°$ is reported, where the sonic line presents an uneven shape. After a series of sanity checks, and further literature research this phenomenon was found to be related with the sonic line transition from the nose towards the aft corner of the capsule. However, this phenomenon is not fully presented in this work since the shoulder expansion is not implemented, an thus, the sonic line does not attach in this region as it is supposed to. Refs. [16–18] present similar phenomena and report that this happens for cone angles larger than θ_s (defined by M_∞ and specific heat ratio γ). This work explored this particularity, gradually varying the cone angle from $45°$ to $60°$. It was found that the sonic line transition starts as soon as $\theta_c \approx 46°$.

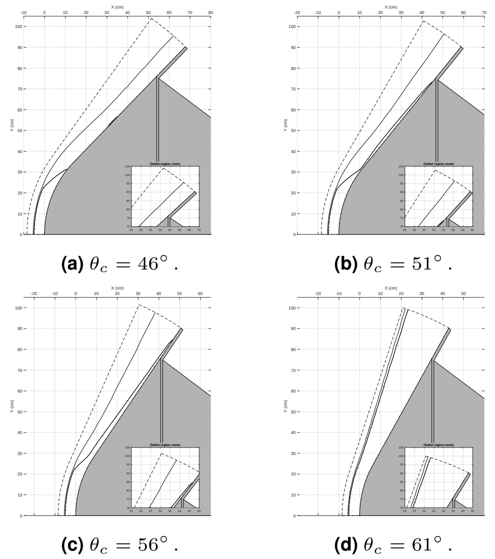

(a) $\theta_c = 46°$. **(b)** $\theta_c = 51°$.

(c) $\theta_c = 56°$. **(d)** $\theta_c = 61°$.

Figure 11: Sonic Lines

Small changes in the angle of attack through the capsule trajectory may reflect in aerodynamic instabilities of the sonic line shifting from the shoulder to the nose cap and back again, specially if the capsule has an angle of attack.

This results turns out to be useful for both TP, resulting in dynamic instabilities even for the case of Entry TP $\theta_c = 60°$ as this phenomenon was already being developed.

For the sake of completeness, the analysis for this case was kept in this work, even though several of the previous assumptions (specifically ignoring the shoulder expansion) no longer stand under this unanticipated behaviour.

5.2. Test Case 2

This test case was firstly intended to evaluate the different shapes considered with different cone angles θ_c and sweep angles η (keeping A_{flap}/A_{main} constant), and check which one is more adequate for an aerocapture maneuver. An aerocapture maneuver is a lifting entry maneuver and requires an angle of attack. However, the results are obtained with a zero-angle of attack, due to our CFD code limitations, and therefore, these results are merely indicative.

Also, as already mentioned before, the results for $\theta_c = 60°$ rely on wrongly made assumptions. Nevertheless, for the sake of completeness, they will still be presented here.

Table 8: Test matrix for Test Case 2

θ_c	Chemical Composition	η	Trajectory Point
60°	A and B	40° ,50° , 60° 70° , 80°	Aerocapture TP
45°	A and B	40° ,50° , 60° 70° , 80°	Aerocapture TP

For $\theta_c = 45°$ a test was made to test the pressure correction function - results with $*$ in Figures 13, 12 and 14. The Mach considered for these corrections was M=3.5, which was the Mach outside the boundary layer in the flap region. For $\theta_c = 60°$, the correction was not used since the flow in this region is not supersonic, making the procedure pointless. When the correction is ignored, for lower η values, the C_L is higher. However, when using the pressure correction, a good part of the flow is near the trim tab tips, which will result in a significant part of the control surface not producing any force. For higher η values, the percentage of the control surface in this area influenced by the tip is lower, which reflects in results closer to the ones when the correction is ignored.

The drag coefficient C_D, presents no sensibility to the sweep angle η, see Figure 12. This is somehow expected since the only difference will be related with the flap as the remaining component from the main body is constant for all cases. The frontal area of the flap is kept constant at a value of 5% of the main body's frontal area. Thus, the projection of the forces in the flap region multiplied by the area will produce always the same force in the x direction, and will result in the same Drag, as the pressure in the flap region is almost constant.

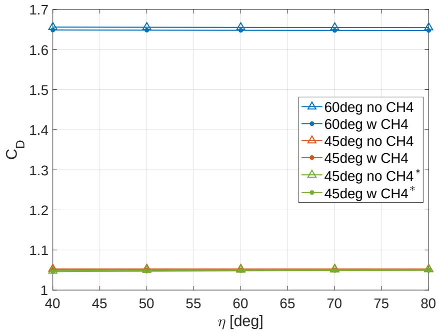

Figure 12: C_D vs η

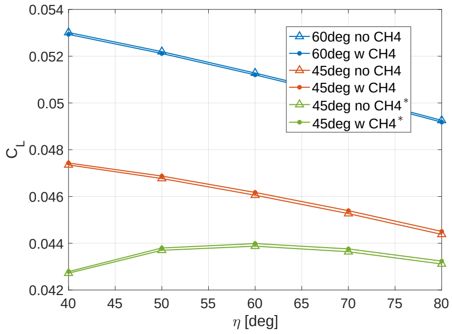

Figure 13: C_L vs η

For the lift, the scenario is different, as the projection of the forces in the y direction will depend not only on θ_c but also on ϕ, and consequently η, see Figure 13.

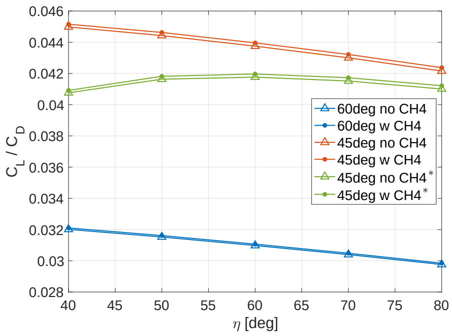

Figure 14: C_L/C_D vs η

Figure 14 shows the aerodynamic efficiency for both cases. This efficiency hits a maximum of 0.041 for $\theta_c = 45°$ both for $\eta = 60°$ and $\eta = 70°$. This is a low value but is expected since this type of capsule is widely use for atmospheric entries, and thus, the main goal is have a high drag to slow down the spacecraft. In this case, the study focused on evaluating the addition of trim tabs to this

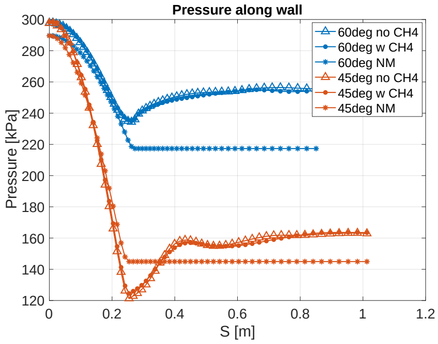

Figure 15: Wall Pressure (CFD & Modified Newtonian theory)

common shape to assess the feasibility of designs like this.

Figure 15 shows the similarities between the Modified Newtonian theory results with CFD results, proving that this method, although very simple and with a great level of approximations, presents a good first estimation for the results in hypersonic flows.

6. Conclusions

The major achievements of this work are the identification on how the low percentage of CH_4 in Neptune's atmosphere ($\approx$ 1.5%) significantly enhances the radiation of the flow. As a reminder, shock tube experiments for similar chemical compositions (Jovian atmosphere with 89% H_2/11 % He) show that radiance for these flows only becomes apparent above 25 km/s. Our numerical results confirm this finding (in the absence of CH_4) since radiative heating is negligible for Entry TP at 18 km/s, but noticeable for the Aerocapture TP at 29 km/s. Once the small fraction of CH_4 is accounted for, the results change dramatically. CH_4 dissociates in the shock layer leading to the formation of hot C and C_2 which strongly radiate in the whole domain. Radiative heating becomes comparable to convective heating even for the Entry TP at 18 km/s, and the Aerocapture TP is impacted as well.

In terms of the total wall heat fluxes for the Entry TP, both designs are more or less equivalent as the 60° geometry minimizes convective heating but maximizes radiative heating. Since both heat fluxes have the same order of magnitude, no clear advantage for a specific geometry may be found in this case. For the Aerocapture TP, the situation is different, as the flow remains subsonic in the shock layer, with an increased shock standoff. This is detrimental in terms of radiative heating, a non local phenomena: a larger volume of the shock layer translates in larger heat fluxes for the 60° geometry. Being so, the 45° configuration is clearly superior in these terms.

In terms of stability, the 45° configuration should be in general more favorable since it is easier to bring the aerodynamic center behind the center of gravity. In addition to this, the 60° configuration was shown to be already in the range of θ_s where instabilities regarding the transition of the sonic line occur. The successful use of control surfaces, such as the trim tab mentioned in this work, becomes even more difficult to achieve for larger angles. 3D simulations should be performed to better analyze these events.

Regarding the use of the trim tab, the aerodynamic analysis concluded that low lift coefficients C_L are achieved, compared to the drag coefficient C_D. However, even with this value being relatively low, it may be enough for generating enough moments since this lifting force will have a corresponding significant moment and will achieve the goal of producing moment and hence angle of attack, without a detriment in mission's available mass.

References

(1) S. Bayon and M. Bandecchi, 2019, ESA CDF Technical Report, 215–231.

(2) R. Jits *et al.*, *Journal of Spacecraft and Rockets*, 2005, **42**, 1025–1034.

(3) C. Park, *Journal of Spacecraft and Rockets*, 2011, **48**, 897–903.

(4) B. R. Hollis *et al.*, *AIAA AFM Conference*, 2004, **2**, 1040–1051.

(5) S. V. Perino *et al.*, *Journal of Spacecraft and Rockets*, 2015, **52**, 1320–1330.

(6) M. Tauber *et al.*, *Flight Simulation and Technologies*, 1994, **31**, 799–805.

(7) J. E. Johnson *et al.*, *Journal of Spacecraft and Rockets*, 2012, **49**, 38–50.

(8) C. Park, *Journal of Spacecraft and Rockets*, 2014, **51**, 635–639.

(9) M. L. Silva, *et al.*, Tech Report, ISTécnico.

(10) T. Gökçen, *Journal of Thermophysics and Heat Transfer*, 2007.

(11) L. P. Leibowitz and T.-j. Kuo, *AIAA Journal*.

(12) G. Palmer and M. J. Wright, 36th AIAA Thermophysics Conference, 2003.

(13) L. Santos Fernandes, Master's Thesis, Instituto Superior Técnico, 2019.

(14) Á. González, *Mathematical Geosciences*.

(15) J. Moss and A. Simmonds, 3rd Joint Thermophysics, Fluids, Plasma and Heat Transfer Conference, 1982, p. 874.

(16) P. A. Gnoffo, *Planetary-entry gas dynamics*, 1999.

(17) J. C. South, *NASA Technical Note*, 1968.

(18) Hornung, H. G. *et al.*, *Journal of Fluid Mechanics*, 2019.